

The National Direct-Drive Program on OMEGA and at the National Ignition Facility

Introduction

The main approach to ignition by means of laser-driven inertial confinement fusion (ICF)¹ currently pursued at the National Ignition Facility (NIF)² is x-ray (or indirect) drive (ID), where the laser energy absorbed in a high-Z hohlraum is re-emitted in the form of x rays that drive the fuel capsule. In the other mainline ICF laser approach, direct drive (DD),³ the target is driven by laser irradiation directly coupled to the plasma ablated from the imploding capsule. The main advantage of ID is reduced sensitivity of implosions to short-scale beam nonuniformities. The main advantage of DD is higher coupling efficiency (by a factor of 3 to 5) of the laser energy into kinetic energy of the shell (hydrodynamic efficiency) compared to that of ID. The OMEGA Laser System⁴ and the KrF laser NIKE at the Naval Research laboratory (NRL)⁵ have been the principal facilities for DD experiments in the U.S. When the decision to pursue ID as the main ICF approach was made by the U.S. ICF program back in 1976, single-beam laser quality was a major concern for achieving high compression in DD implosions without the shell breaking apart from the Rayleigh–Taylor (RT) instability¹ seeded by laser imprint. Early challenges in improving beam uniformity have been resolved over the last several decades by introducing several beam-smoothing techniques. These include distributed phase plates (DPP's),⁶ polarization smoothing with birefringent wedges,⁷ and smoothing by spectral dispersion (SSD).⁸ In addition, implementing adiabat-shaping techniques^{9,10} significantly reduced the impact of RT instability growth during shell acceleration. Also, imprint reduction was demonstrated by using mid-Z-doped ablaters¹¹ and high-Z target overcoats.¹² Such progress along with the challenges in achieving ignition on the NIF using ID¹³ suggests considering direct drive as a viable alternative for developing a burning-plasma platform in a laboratory. In addition to the conventional “hot-spot” ignition designs, several alternative direct-drive-ignition schemes have been proposed in the past. Shock ignition,¹⁴ the most-promising approach, is currently being considered as an alternative symmetric direct-drive-ignition design for the NIF.

Compared to x-ray drive, direct-drive targets couple a larger fraction of laser energy into shell kinetic energy and internal energy of the neutron-producing central region of the target (hot spot) at peak fuel compression. This relaxes the requirement on shell convergence and hot-spot pressure in an igniting target. The ignition condition follows from Lawson criterion,^{15,16} which can be written in a form commonly used in the ICF community as¹

$$(\rho R)_{\text{hs}} \times T \gtrsim 0.3 \text{ g/cm}^3 \times 5 \text{ keV}, \quad (1)$$

where ρ , R_{hs} , and T are the hot-spot density, radius, and ion temperature, respectively. The requirement shown in Eq. (1) is intuitively simple: the hot-spot temperature must be ~ 5 keV for PdV work of the incoming shell to overcome radiation losses and have an alpha-particle production rate sufficient to create bootstrap heating; an areal density of $\sim 0.3 \text{ g/cm}^2$ is required to stop alpha particles inside the hot spot at these temperatures. A product of these two quantities enters into the ignition condition since ignition at lower temperatures and higher areal densities is still possible because the cold shell becomes more opaque to radiation at higher shell areal densities (assuming that larger hot-spot areal density leads to larger shell areal densities), limiting radiation losses from the hot spot.¹⁶ Substituting expressions for the pressure $p_{\text{hs}} = (1 + Z)\rho T/m_i$ (Z is the average ion charge and m_i is the average ion mass) and internal energy $E_{\text{hs}} = 3/2 p_{\text{hs}} V_{\text{hs}}$ (V_{hs} is the neutron-averaged hot-spot volume) into Eq. (1) gives a minimum pressure requirement (threshold) for ignition:

$$p_{\text{hs}} > p_{\text{thr}} \equiv 250 \text{ Gbar} \left(\frac{E_{\text{hs}}}{10 \text{ kJ}} \right)^{-1/2},$$

or

$$\bar{P} \equiv \frac{p_{\text{hs}}}{p_{\text{thr}}} = \left(\frac{p_{\text{hs}}}{250 \text{ Gbar}} \right) \sqrt{\frac{E_{\text{hs}}}{10 \text{ kJ}}} > 1, \quad (2)$$

where \bar{P} is the ignition pressure parameter. Equation (2) also sets the limit on the hot-spot volume in an igniting target:

$$V_{\text{hs}} < V_{40} \left(\frac{E_{\text{hs}}}{10 \text{ kJ}} \right)^{3/2}, \text{ or } \max(R_{\text{hs}}) \sim \sqrt{E_{\text{hs}}}, \quad (3)$$

where $V_{40} = 4\pi/3 (40 \mu\text{m})^3$ is the volume of a 40- μm sphere. Figure 148.6 plots the alpha-amplification factor ($Y_\alpha/Y_{\text{no}\alpha} - 1$, where Y_α and $Y_{\text{no}\alpha}$ are the target yields with and without alpha-particle deposition and fuel heating, respectively) as a function of ignition pressure parameter \bar{P} . The plot is obtained using 1-D *LILAC*¹⁷ simulations of cryogenic targets at different laser drive energies (from OMEGA- to the NIF-scale designs). The solid line in the figure shows a fit to the simulation results at $\bar{P} < 1$, $\delta Y/Y = \bar{P} \exp(1.7 \bar{P}^{2/3})$. $\bar{P} \sim 1$ defines the ignition threshold. When $\bar{P} > 1$ and the fuel areal density at peak compression is large enough [$(\rho R)_{\text{fuel}} > 1 \text{ g/cm}^2$] to burn a significant fraction of the main fuel, the target gain greatly exceeds unity ($G > 10$). In simulations where the main fuel areal density is low, the shell burnup fraction is not significant and the yield amplification continues to follow the fit even for $\bar{P} > 1$.

Spherically symmetric DD cryogenic designs on OMEGA presently couple up to 0.44 kJ (out of 26-kJ incident laser energy) into the hot-spot internal energy.¹⁸ When hydrodynamically scaled to the NIF-size laser energy (1.5 MJ to

1.8 MJ), these designs are predicted to couple $5\times$ to $10\times$ more energy into the hot spot [25 kJ to 40 kJ for DD designs, depending on the laser-coupling efficiency] compared to that of ID (4 kJ to 5 kJ is inferred in the current best-performing ID implosions on the NIF), resulting in $2.5\times$ to $3\times$ lower hot-spot pressures required for DD ignition. The hot-spot size also gets larger with E_{hs} [see Eq. (3)], leading to smaller shell convergence ratio (CR ~ 22 compared to 35 to 40 in the ID ignition designs) and resulting in less-demanding long-wavelength drive-uniformity requirements.

With the goal of a successful ignition demonstration using direct drive, the recently established national DD strategy has several elements and involves the following facilities and institutions: Omega (a leading facility for DD research); NRL [which leads the effort on laser imprint reduction and plays a major role in the mitigation of coupling losses caused by laser-plasma interaction (LPI)]; Lawrence Livermore National Laboratory (which recently established a DD working group concentrating its effort on understanding LPI at ignition-relevant scales, developing DD target designs with yields in the range from 100 kJ to a few MJ, and developing 3-D computational capability for DD applications); and Los Alamos National Laboratory (which leads the effort in simulating high-Z overcoats, experimental study of long-wavelength drive asymmetry, and developing platforms to study material properties in the warm-dense-matter regime). The elements of DD strategy include experimentally demonstrating on OMEGA the hot-spot conditions ($p_{\text{hs}} > 100 \text{ Gbar}$) relevant for ignition at MJ-scale laser energies available on the NIF and developing an understanding of LPI and laser coupling using DD experiments on the NIF in the current indirect-drive configuration.

OMEGA Cryogenic Implosions

The target performance depends on both the drive and uniformity conditions. We begin this section with a discussion on the one-dimensional (1-D) physics.

1. One-Dimensional Physics

To emphasize the importance of drive conditions in designing ignition targets, the 1-D scaling laws (which exclude multi-dimensional effects) for peak pressure and hot-spot energy are written in terms of implosion parameters: implosion velocity v_{imp} (the peak mass-averaged shell velocity), peak drive (ablation) pressure p_{abl} , adiabat α of the unablated fuel mass (ratio of the shell pressure to Fermi pressure at shell density), and peak in shell kinetic energy E_{kin} (Ref. 19):

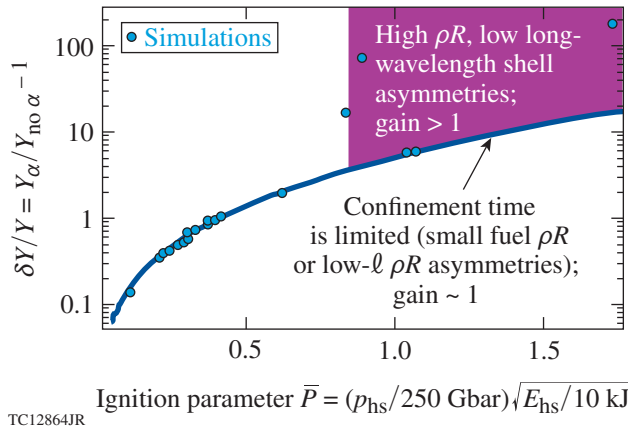


Figure 148.6 Alpha-amplification factor $\delta Y/Y$ as function of the ignition pressure parameter \bar{P} . The points represent the results of 1-D *LILAC* simulations of designs at different laser energies in the range of OMEGA to National Ignition Facility (NIF) scale. The solid line shows a fit to the simulation results at $\bar{P} < 1$, $\delta Y/Y = \bar{P} \exp(1.7 \bar{P}^{2/3})$.

$$\begin{aligned}
 P_{\text{hs}}^{1\text{-D}} &\sim \frac{p_{\text{abl}}^{1/3} v_{\text{imp}}^{10/3}}{\alpha}, \\
 E_{\text{hs}}^{1\text{-D}} &\sim E_{\text{kin}} \frac{v_{\text{imp}}^{4/3}}{\alpha^{2/5} p_{\text{abl}}^{4/15}}, \\
 \bar{P}^{1\text{-D}} &\sim \frac{\sqrt{E_{\text{kin}}} v_{\text{imp}}^4 p_{\text{abl}}^{1/5}}{\alpha^{6/5}}. \quad (4)
 \end{aligned}$$

Modeling these critical implosion parameters must be experimentally validated before an assessment of the importance of multidimensional effects on the target performance can be made. The implosion velocity and shell kinetic energy are inferred in an experiment by measuring ablation-front trajectory and mass ablation rate using self-emission imaging.²⁰ The ablation pressure is inferred from simulations that match the measured ablation-front trajectory, mass ablation rate, bang time,²¹ and scattered-light power and spectrum.^{19,22} Finally, the shock-induced adiabat is inferred by measuring shock velocities early in the pulse using the velocity interferometer system for any reflector (VISAR).²³ An additional increase in the fuel adiabat caused by hot-electron preheat is estimated by measuring the hard x-ray signal²⁴ and areal density^{25,26} in mid- to high-adiabat implosions (the areal density in 1-D, for a given laser energy, depends mainly on shell adiabat,²⁷ $\rho R \sim \alpha^{-0.5}$). A detailed comparison of 1-D simulation results using *LILAC* with the data shows good agreement between the two for a variety of target designs and drive conditions.¹⁹ One-dimensional simulations include a nonlocal thermal-transport model,²⁸ a ray-based cross-beam energy transfer (CBET) model²⁹ (see discussion on CBET in **Laser Coupling and CBET**, p. 177), and first-principles equation-of-state (FPEOS) models³⁰ for both the DT ice and CD ablator.

2. Multidimensional Effects

The stability properties of indirect- and direct-drive designs are different. In direct drive, a thin CH layer is ablated from the shell early in the pulse to take advantage of the higher hydrodynamic efficiency of DT.¹⁹ Since the shell consists mainly of DT during acceleration, the fuel adiabat α [which enters into the ignition scaling laws shown in Eqs. (4)] and the average in-flight shell adiabat α_{shell} (which determines shell stability property) are approximately equal, $\alpha \sim \alpha_{\text{shell}}$ ($\alpha_{\text{shell}} \gtrsim \alpha$ in adiabat-shaped designs¹⁰). Then, the shell's in-flight aspect ratio (IFAR, defined as ratio of the target radius to the shell thickness) can be written as³¹

$$\text{IFAR}_{\text{DD}} \sim \frac{v_{\text{imp}}^2}{(p_{\text{abl}}^{2/5} \alpha_{\text{shell}}^{3/5})} \sim \frac{v_{\text{imp}}^2}{(p_{\text{abl}}^{2/5} \alpha^{3/5})}. \quad (5)$$

While the in-flight shell adiabat in DD designs is determined primarily by the strength of initial shocks (the radiation preheat in DD cryogenic implosions raises the fuel adiabat by ~20%), the shell adiabat and IFAR in ID designs are determined mainly by the radiation transport, ablator opacity, and x-ray drive spectrum (the majority of shell mass during acceleration in indirect drive consists of the ablator material; ablator and main fuel masses become approximately equal at the end of acceleration). As a result,

$$\text{IFAR}_{\text{ID}} \approx \frac{v_{\text{imp}}^2}{(p_{\text{abl}}^{2/5} \alpha_{\text{shell}}^{3/5})}. \quad (6)$$

Note that even though IFAR and the ablation-front RT growth in ID are determined by the x-ray heating of the ablator and not by the strength of initial shocks, the initial condition for RT instability is set during the shock propagation through the shell early in the drive, the so-called Richtmyer–Meshkov (RM) phase of perturbation evolution.³² Therefore, the difference in the stability properties of indirectly driven shells for $\alpha = 1.4$ and “high-foot” $\alpha = 2.5$ designs¹³ is caused mainly by differences in nonuniformity growth during the RM phase.³³

Substituting Eq. (5) into Eq. (4) gives the following hot-spot scaling laws for DD implosions:

$$\begin{aligned}
 P_{\text{hs}}^{1\text{-D}} &\sim p_{\text{abl}} \text{IFAR}^{5/3}, \\
 V_{\text{hs}}^{1\text{-D}} &\sim \frac{E_{\text{kin}}}{p_{\text{abl}} \text{IFAR}}, \\
 E_{\text{hs}}^{1\text{-D}} &\sim E_{\text{kin}} \text{IFAR}^{2/3}, \\
 \bar{P}^{1\text{-D}} &\sim p_{\text{abl}} \sqrt{E_{\text{kin}}} \text{IFAR}^2. \quad (7)
 \end{aligned}$$

Equations (7) shows that the hot-spot pressure and the ignition pressure parameter \bar{P} can be increased in 1-D mainly by raising the shell IFAR (by reducing the shell mass, for example) and by making the laser drive more efficient (by increasing the ablation pressure and shell kinetic energy). The maximum value of IFAR in a design is set by the target stability properties and the level of nonuniformity seeds: the short-scale modes (which

satisfy $k\Delta < 1$, where k is the perturbation wave number and Δ is the in-flight shell thickness) disrupt the shell during the implosion if IFAR is too large [current cryogenic implosions on OMEGA are unstable if $\text{IFAR} > 20$ ($\alpha/3$)^{1,1} (Ref. 19)]. The long-wavelength perturbations ($k\Delta > 1$) seeded by the laser power imbalance, laser mispointing, and target misalignment can prevent the hot spot from reaching the 1-D stagnation pressures if the RT instability and Bell–Plesset (BP)¹ nonuniformity growth are excessively large during deceleration. The design IFAR can be increased, nevertheless, if (1) the short-scale nonuniformities seeded by target imperfections and imprint are reduced and (2) the source of the long-wavelength perturbations (beam imbalance, target offset, and beam mispointing) is minimized.

3. Target Performance

Figure 148.7 shows the scaled ignition pressure parameter \bar{P} inferred in OMEGA cryogenic implosions. Since v_{imp} , p_{abl} , and α are invariants with respect to laser energy E_L and E_{kin} is proportional to E_L (assuming constant laser-coupling efficiency for different E_L), \bar{P} scales as $\sqrt{E_{\text{kin}}}$ [see Eq. (2)]. Therefore, extrapolating the OMEGA results to the NIF-scale laser energy leads to $\bar{P}_{\text{scaled}} = \bar{P}_{\text{OMEGA}} (E_L^{\text{NIF}} / E_L^{\text{OMEGA}})^{1/2}$.

The latter quantity is plotted in Fig. 148.7 for OMEGA cryogenic implosions driven at different values of the fuel adiabat (calculated using *LILAC* simulations). The hot-spot pressure and

internal energy are inferred^{18,34} by using the measured neutron yield, the burn duration Δt_{burn} (Ref. 21), the neutron-averaged ion temperature $\langle T_i \rangle_n$, and the hot-spot size. Diamonds represent the experimentally inferred \bar{P}_{scaled} and squares represent the 1-D *LILAC* predictions. The trend lines represent the best linear fit to the simulation data. The highest hot-spot pressure inferred in these experiments is 56 ± 7 Gbar (Ref. 18). According to Fig. 148.7, when scaled to the laser energy available on the NIF, the current OMEGA implosions reach up to $\sim 40\%$ of the pressure required for ignition. Then, using the alpha amplification scaling shown in Fig. 148.6, these implosions would yield a $2\times$ yield amplification because of alpha heating. Similar conclusions were reached using an independent calculation recently performed based on the $P\tau$ analysis.³⁵

To understand the trends shown in Fig. 148.7, the effects of shell nonuniformity must be considered. As the shell adiabat increases, the target performance becomes less sensitive to the nonuniformity growth and the inferred \bar{P} approaches the 1-D-predicted values. For lower values of shell adiabat, however, the deviation of the observed \bar{P} from the predictions increases. Since the 1-D value of \bar{P} decreases with the adiabat [see Eq. (4)], the inferred value has a maximum at $\alpha \sim 3.5$, which is a consequence of the interplay between a 1-D reduction in \bar{P} and a shell stability improvement as the adiabat increases.

The performance-degradation mechanisms in cryogenic DD implosions include both the long-wavelength modes and the short-scale growth (which breaks up the shell during acceleration and introduces mix between the ablator and the hot spot as well as between the cold, denser part of the fuel and the hot spot). The long-wavelength modes increase the volume of a central, lower-density region (which forms the hot spot when the effects of asymmetry growth are negligible but might contain colder regions excluded from the hot spot in a perturbed implosion) as well as create thin spots in the cold shell during deceleration, producing expanding bubbles that reduce pusher efficiency and limit hot-spot confinement.^{18,36}

4. Three-Dimensional Results

The evolution of long-wavelength nonuniformities seeded by the target offset, beam geometry, beam-power imbalance, and mispointing is studied using the 3-D hydrocode *ASTER*.³⁶ These simulations show that such nonuniformities form bubbles (regions of low-density material that protrude from the central region into the higher-density shell) that develop because of the deceleration in RT and BP growth. As the shell continues to converge, the bubbles eventually break out of the shell, prematurely quenching the hot-spot confinement and neutron

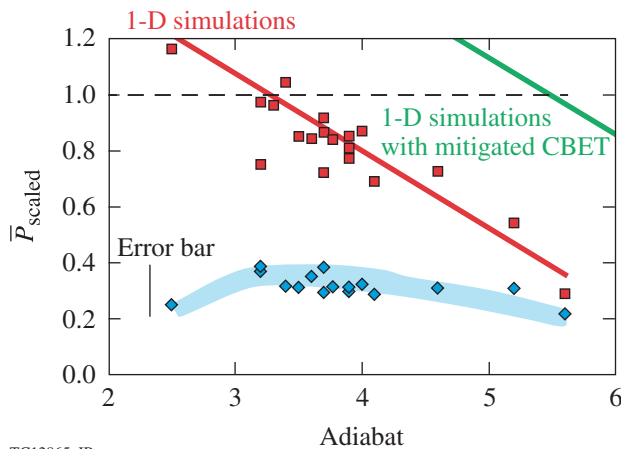


Figure 148.7 Ignition pressure parameter scaled to 1.8-MJ laser energy. Diamonds represent values inferred from the experimental data, squares show the 1-D simulation results with the full cross-beam energy transfer (CBET) effect, and the solid green line represents a linear fit through simulations with CBET fully mitigated. The short vertical line shows a typical error bar for the inferred values of \bar{P} . To ignite, \bar{P}_{scaled} in a design must exceed unity (dashed line).

yield.^{34,36} Because nonuniformities cause the peak burn to occur earlier, our observations based on the fusion products sample the implosion conditions when the shell convergence has not yet reached the peak value. This effect and nonradial flows caused by the 3-D effects prevent the fuel from reaching stagnation, limiting conversion efficiency of shell kinetic energy into internal energy of the hot spot at peak burn.

The experimental evidence of low-mode asymmetries includes the x-ray self-emission imaging from a tracer Ti layer embedded into the CH shell.³⁷ This technique shows that significant low-mode nonuniformities developed during deceleration. Another self-emission imaging technique that maps the implosion shape during the acceleration indicates the growth of low- ℓ modes while the target is being driven by laser illumination.³⁸ In addition, significant variations in the measured ion temperature along different lines of sight (LOS's) in cryogenic implosions are also indicative of asymmetry flows. The ion temperature is inferred in an experiment by measuring the spectral width of neutrons created as a result of fusing D and T. The spectral broadening, however, is caused not only by the thermal effects but also by the bulk motion with velocity distribution not aligned in a single direction. This results in higher temperature inferred from the fit $\langle T \rangle_{\text{fit}}$ compared to the true thermal ion temperature T (Refs. 31 and 39): $\langle T \rangle_{\text{fit}} \simeq T + 2/3 m_i V_f^2$, where m_i is the average mass of fusion-reaction products and V_f is the bulk velocity. Since asymmetry growth creates different V_f along different LOS's, different values of ion temperature are inferred along multiple LOS's in a highly distorted implosion. The maximum measured temperature difference along three LOS's in OMEGA cryogenic implosions is shown in Fig. 148.8(a). The inferred temperature differences, up to 1 keV, correspond to nonradial flow velocities of $V_f \sim 2.5 \times 10^7$ cm/s. This is consistent with the results of 3-D *ASTER* simulations that include the effect of power imbalance and target offset. The plot in Fig. 148.8(b) shows the calculated neutron spectra at three perpendicular views (solid lines) together with neutron spectrum calculated without the effect of bulk motion (dashed line). Figure 148.8(a) also shows that the measured temperature variation strongly correlates with the yield degradation relative to the 1-D predictions, suggesting that the residual kinetic energy plays a detrimental role in reducing the target performance.

The performance degradation in lower-adiabat implosions ($\alpha < 2.5$) is caused by both the long wavelengths (as described above) and the short-scale nonuniformities. The latter are seeded mainly by laser imprint, nonuniformities caused by target fabrication, and debris accumulated during cryogenic

target production. Simulations indicate that the surface defects are the most damaging since they quickly evolve into nonlinear bubbles (modulations that produce local depressions in shell density) at the ablation front that are not stabilized by ablation⁴⁰ and grow at a rate exceeding the classical limit. Such growth leads to the ablator mixing into the main fuel and the vapor region.⁴¹ These effects are directly observed in experiments. The ablator/cold shell mix is inferred from the backlit images obtained using a monochromatic x-ray imager.⁴² The observed enhancement in x-ray attenuation by the main fuel in the low-adiabat implosion, not predicted by 1-D calculations,

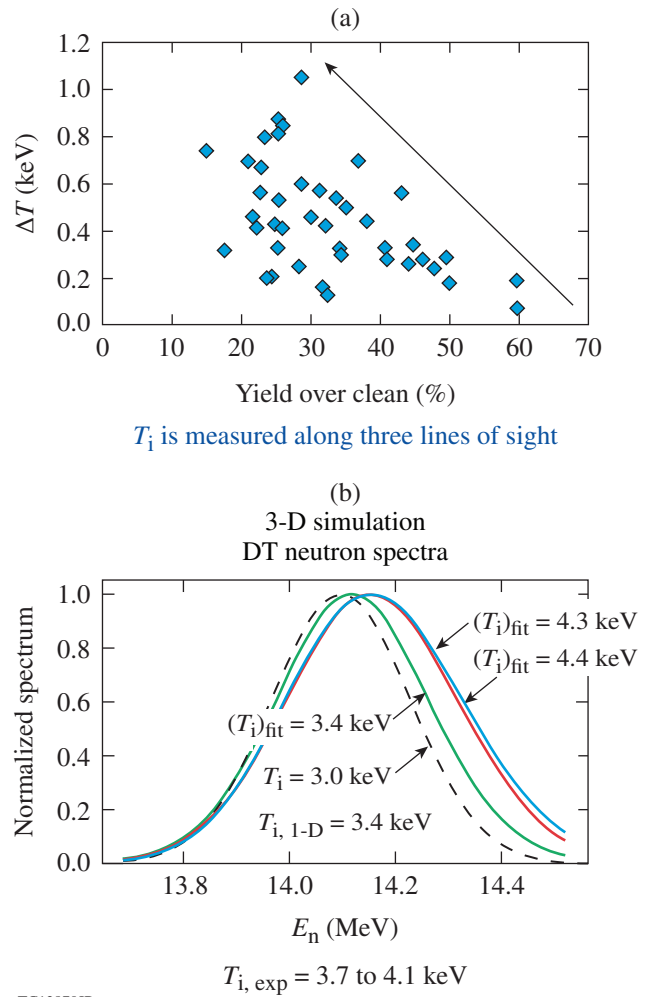


Figure 148.8 (a) The measured variation in ion temperature ΔT (keV) among three lines of sight in cryogenic implosions on OMEGA as a function of yield-over-predictions. (b) Neutron spectra along three perpendicular views (solid lines) as calculated using *ASTER* simulations of an OMEGA cryogenic implosion assuming ~ 20 - μm target offset and 15%-root-mean-square (rms) power imbalance. The dashed line shows the neutron spectrum without the effects of the bulk fuel motion.

is consistent with 0.1% to 0.2% atomic mixing of C into DT. No mixing is required to explain the observed fuel opacity in higher-adiabat implosions ($\alpha > 3.5$). In addition, the x-ray core emission at peak compression is also enhanced when the fuel adiabat is reduced to $\alpha < 2.5$, indicating that ablator carbon penetrates all the way into the hot spot during the implosion.⁴³ The plastic ablator in direct-drive designs is thin and gets ablated in the middle of the drive pulse. The presence of the ablator in the hot spot suggests therefore a significant growth in local surface features that produce jet-like structures in the shell early in the implosion and bring the ablator material into the hot spot.⁴¹

5. Laser Coupling and CBET

The shell’s stability properties can be significantly improved by increasing laser coupling and making the shell thicker. This can be accomplished by increasing the drive hydroefficiency. An analysis of direct-drive implosions on OMEGA has shown that coupling losses related to CBET²⁹ significantly limit the ablation pressure (as much as 40% on OMEGA and up to 60% on NIF-scale targets), implosion velocity, and shell kinetic energy. CBET results from the scattering of incoming laser light caused by stimulated Brillouin scatter. The reduction in the ablation pressure caused by CBET is shown in Fig. 148.9, where the ablation pressure, calculated at the time when the ablation surface had converged by a factor of 2.5, is plotted for OMEGA and NIF-scale symmetric designs at different drive intensities. Considering such losses, demonstrating the hydrodynamic equivalence of implosions on OMEGA to ignition designs on the NIF requires the shell IFAR to exceed the current stability threshold level (~22) (Ref. 19).

One of the CBET mitigation strategies⁴⁴ involves reducing the laser beam size relative to the initial target size. This strategy, as demonstrated both theoretically and experimentally, recovers some coupling losses and increases the ablation

pressure.^{29,34,45} The benefit of reducing beam size to enhance laser coupling is illustrated in Fig. 148.10, where the predicted time-dependent ablation pressure (plotted as a function of shell convergence) is shown for different ratios of R_b/R_t (R_b is defined as the radius of a 95% beam-energy contour). Figure 148.10 shows that the largest increase in coupling occurs early in the implosion when the critical surface is at a larger radius and the refraction effects prevent beams from intersecting in regions where CBET is effective (Mach ~ 1 surface in plasma corona). Later in the implosion when the critical surface has moved inward a sufficient distance, beams start to intersect in the CBET-resonant regions and exchange their energy, increasing CBET losses. When CBET is fully mitigated, the shell’s kinetic and hot-spot internal energies increase, allowing implosions to reach ignition condition at a higher adiabat. This is illustrated in Fig. 148.7, where the green trend line shows the ignition pressure parameter with the enhanced laser

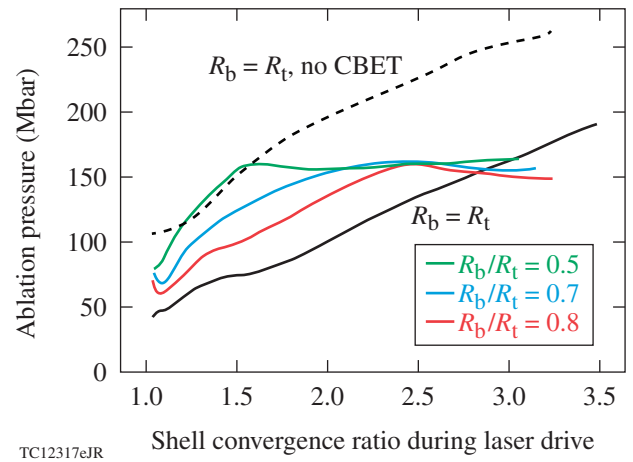


Figure 148.10 Time-dependent ablation pressure as a function of shell convergence for designs driven at $I = 9 \times 10^{14} \text{ W/cm}^2$.

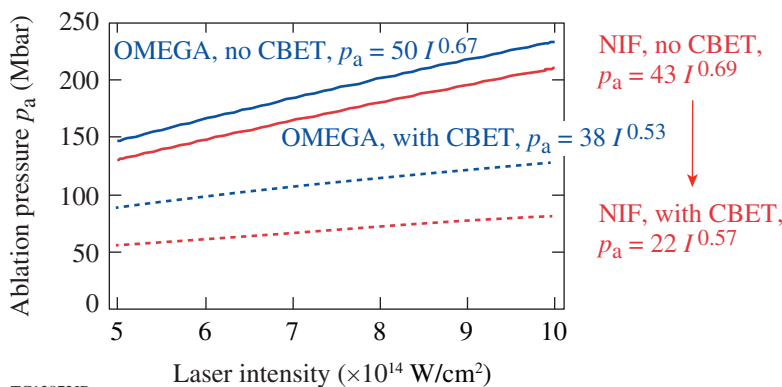


Figure 148.9 Ablation pressure as a function of incident laser intensity for OMEGA and NIF-scale designs. Solid lines show the calculation results without the effect of CBET; dashed lines include the effect of CBET. The ablation pressure was calculated when the ablation front had converged by a factor of 2.5 from its initial radius.

TC12872JR

coupling. The adiabat in the ignition designs can be increased in this case up to $\alpha \sim 5.5$, significantly improving the shell's stability properties.

Experimental campaigns performed on OMEGA with the reduced R_b/R_t have demonstrated increased hydrodynamic efficiency.³⁴ The target performance in such implosions, however, was degraded. This was explained, based on the results of 3-D *DASTER* simulations,³⁶ by asymmetries caused by power imbalance, enhanced in these implosions because of reduced beam overlap.

Conclusions

The direct-drive approach to ignition, when compared to indirect-drive designs, offers a significant increase (by a factor of 3 to 5) in laser coupling to the shell kinetic energy. Cryogenic implosions on OMEGA have reached hot-spot pressures of 56 Gbar, which is $\sim 40\%$ of what is required for ignition. Extrapolating these results to NIF-scale laser energy is predicted to enhance the yield caused by alpha heating by a factor of 2. The cryogenic campaigns with reduced beam size relative to the target size ($R_b/R_t < 1$), performed on OMEGA to reduce CBET losses, demonstrated increased laser coupling and hydrodynamic efficiency; however, this coupling enhancement did not improve the target performance. Numerical simulations indicate that long-wavelength nonuniformities caused by target offset and power imbalance lead to an increased target central volume and early burn truncation. Reaching the goal of demonstrating hydrodynamic equivalence on OMEGA must include improving laser power balance, target position, and target quality at shot time. CBET must also be reduced to increase the fuel mass and improve shell stability. CBET mitigation strategies include reduction in the beam size relative to the target size and laser wavelength separation.⁴⁶

ACKNOWLEDGMENT

This material is based upon work supported by the Department of Energy National Nuclear Security Administration under Award Number DE-NA0001944, the University of Rochester, and the New York State Energy Research and Development Authority. The support of DOE does not constitute an endorsement by DOE of the views expressed in this article.

REFERENCES

1. S. Atzeni and J. Meyer-ter-Vehn, *The Physics of Inertial Fusion: Beam Plasma Interaction, Hydrodynamics, Hot Dense Matter*, International Series of Monographs on Physics (Clarendon Press, Oxford, 2004).
2. J. Paisner *et al.*, *Laser Focus World* **30**, 75 (1994).
3. R. S. Craxton, K. S. Anderson, T. R. Boehly, V. N. Goncharov, D. R. Harding, J. P. Knauer, R. L. McCrory, P. W. McKenty, D. D. Meyerhofer, J. F. Myatt, A. J. Schmitt, J. D. Sethian, R. W. Short, S. Skupsky, W. Theobald, W. L. Kruer, K. Tanaka, R. Betti, T. J. B. Collins, J. A. Delettrez, S. X. Hu, J. A. Marozas, A. V. Maximov, D. T. Michel, P. B. Radha, S. P. Regan, T. C. Sangster, W. Seka, A. A. Solodov, J. M. Soures, C. Stoeckl, and J. D. Zuegel, *Phys. Plasmas* **22**, 110501 (2015).
4. T. R. Boehly, D. L. Brown, R. S. Craxton, R. L. Keck, J. P. Knauer, J. H. Kelly, T. J. Kessler, S. A. Kumpan, S. J. Loucks, S. A. Letzring, F. J. Marshall, R. L. McCrory, S. F. B. Morse, W. Seka, J. M. Soures, and C. P. Verdon, *Opt. Commun.* **133**, 495 (1997).
5. S. P. Obenschain *et al.*, *Phys. Plasmas* **3**, 2098 (1996).
6. T. J. Kessler, Y. Lin, J. J. Armstrong, and B. Velazquez, *Proc. SPIE* **1870**, 95 (1993).
7. T. R. Boehly, V. A. Smalyuk, D. D. Meyerhofer, J. P. Knauer, D. K. Bradley, R. S. Craxton, M. J. Guardalben, S. Skupsky, and T. J. Kessler, *J. Appl. Phys.* **85**, 3444 (1999).
8. S. Skupsky, R. W. Short, T. Kessler, R. S. Craxton, S. Letzring, and J. M. Soures, *J. Appl. Phys.* **66**, 3456 (1989).
9. V. N. Goncharov, J. P. Knauer, P. W. McKenty, P. B. Radha, T. C. Sangster, S. Skupsky, R. Betti, R. L. McCrory, and D. D. Meyerhofer, *Phys. Plasmas* **10**, 1906 (2003).
10. V. N. Goncharov, T. C. Sangster, T. R. Boehly, S. X. Hu, I. V. Igumenshchev, F. J. Marshall, R. L. McCrory, D. D. Meyerhofer, P. B. Radha, W. Seka, S. Skupsky, C. Stoeckl, D. T. Casey, J. A. Frenje, and R. D. Petrasso, *Phys. Rev. Lett.* **104**, 165001 (2010).
11. S. X. Hu, G. Fiksel, V. N. Goncharov, S. Skupsky, D. D. Meyerhofer, and V. A. Smalyuk, *Phys. Rev. Lett.* **108**, 195003 (2012).
12. S. P. Obenschain *et al.*, *Phys. Plasmas* **9**, 2234 (2002).
13. O. A. Hurricane *et al.*, *Nature* **506**, 343 (2014).
14. R. Betti, C. D. Zhou, K. S. Anderson, L. J. Perkins, W. Theobald, and A. A. Solodov, *Phys. Rev. Lett.* **98**, 155001 (2007).
15. J. D. Lawson, *Proc. Phys. Soc. Lond. B* **70**, 6 (1957).
16. R. Betti, P. Y. Chang, B. K. Spears, K. S. Anderson, J. Edwards, M. Fatenejad, J. D. Lindl, R. L. McCrory, R. Nora, and D. Shvarts, *Phys. Plasmas* **17**, 058102 (2010).
17. J. Delettrez, R. Epstein, M. C. Richardson, P. A. Jaanimagi, and B. L. Henke, *Phys. Rev. A* **36**, 3926 (1987).
18. S. P. Regan, V. N. Goncharov, I. V. Igumenshchev, T. C. Sangster, R. Betti, A. Bose, T. R. Boehly, M. J. Bonino, E. M. Campbell, D. Cao, T. J. B. Collins, R. S. Craxton, A. K. Davis, J. A. Delettrez, D. H. Edgell, R. Epstein, C. J. Forrest, J. A. Frenje, D. H. Froula, M. Gatu Johnson, V. Yu. Glebov, D. R. Harding, M. Hohenberger, S. X. Hu, D. Jacobs-Perkins, R. T. Janezic, M. Karasik, R. L. Keck, J. H. Kelly, T. J. Kessler,

- J. P. Knauer, T. Z. Kosc, S. J. Loucks, J. A. Marozas, F. J. Marshall, R. L. McCrory, P. W. McKenty, D. D. Meyerhofer, D. T. Michel, J. F. Myatt, S. P. Obenshain, R. D. Petrasso, R. B. Radha, B. Rice, M. Rosenberg, A. J. Schmitt, M. J. Schmitt, W. Seka, W. T. Shmayda, M. J. Shoup III, A. Shvydky, S. Skupsky, S. Solodov, C. Stoeckl, W. Theobald, J. Ulreich, M. D. Wittman, K. M. Woo, B. Yaakobi, and J. D. Zuegel, *Phys. Rev. Lett.* **117**, 025001 (2016).
19. V. N. Goncharov, T. C. Sangster, R. Betti, T. R. Boehly, M. J. Bonino, T. J. B. Collins, R. S. Craxton, J. A. Delettrez, D. H. Edgell, R. Epstein, R. K. Follet, C. J. Forrest, D. H. Froula, V. Yu. Glebov, D. R. Harding, R. J. Henchen, S. X. Hu, I. V. Igumenshchev, R. Janezic, J. H. Kelly, T. J. Kessler, T. Z. Kosc, S. J. Loucks, J. A. Marozas, F. J. Marshall, A. V. Maximov, R. L. McCrory, P. W. McKenty, D. D. Meyerhofer, D. T. Michel, J. F. Myatt, R. Nora, P. B. Radha, S. P. Regan, W. Seka, W. T. Shmayda, R. W. Short, A. Shvydky, S. Skupsky, C. Stoeckl, B. Yaakobi, J. A. Frenje, M. Gatu-Johnson, R. D. Petrasso, and D. T. Casey, *Phys. Plasmas* **21**, 056315 (2014).
 20. D. T. Michel, C. Sorce, R. Epstein, N. Whiting, I. V. Igumenshchev, R. Jungquist, and D. H. Froula, *Rev. Sci. Instrum.* **83**, 10E530 (2012).
 21. C. Stoeckl, V. Yu. Glebov, S. Roberts, T. C. Sangster, R. A. Lerche, R. L. Griffith, and C. Sorce, *Rev. Sci. Instrum.* **74**, 1713 (2003).
 22. W. Seka, D. H. Edgell, J. P. Knauer, J. F. Myatt, A. V. Maximov, R. W. Short, T. C. Sangster, C. Stoeckl, R. E. Bahr, R. S. Craxton, J. A. Delettrez, V. N. Goncharov, I. V. Igumenshchev, and D. Shvarts, *Phys. Plasmas* **15**, 056312 (2008).
 23. L. M. Barker and R. E. Hollenbach, *J. Appl. Phys.* **43**, 4669 (1972).
 24. C. Stoeckl, V. Yu. Glebov, D. D. Meyerhofer, W. Seka, B. Yaakobi, R. P. J. Town, and J. D. Zuegel, *Rev. Sci. Instrum.* **72**, 1197 (2001).
 25. J. A. Frenje, C. K. Li, F. H. Séguin, D. T. Casey, R. D. Petrasso, T. C. Sangster, R. Betti, V. Yu. Glebov, and D. D. Meyerhofer, *Phys. Plasmas* **16**, 042704 (2009).
 26. C. J. Forrest, P. B. Radha, V. Yu. Glebov, V. N. Goncharov, J. P. Knauer, A. Pruyne, M. Romanofsky, T. C. Sangster, M. J. Shoup III, C. Stoeckl, D. T. Casey, M. Gatu-Johnson, and S. Gardner, *Rev. Sci. Instrum.* **83**, 10D919 (2012).
 27. R. Betti and C. Zhou, *Phys. Plasmas* **12**, 110702 (2005).
 28. V. N. Goncharov, T. C. Sangster, P. B. Radha, R. Betti, T. R. Boehly, T. J. B. Collins, R. S. Craxton, J. A. Delettrez, R. Epstein, V. Yu. Glebov, S. X. Hu, I. V. Igumenshchev, J. P. Knauer, S. J. Loucks, J. A. Marozas, F. J. Marshall, R. L. McCrory, P. W. McKenty, D. D. Meyerhofer, S. P. Regan, W. Seka, S. Skupsky, V. A. Smalyuk, J. M. Soures, C. Stoeckl, D. Shvarts, J. A. Frenje, R. D. Petrasso, C. K. Li, F. Séguin, W. Manheimer, and D. G. Colombant, *Phys. Plasmas* **15**, 056310 (2008).
 29. I. V. Igumenshchev, D. H. Edgell, V. N. Goncharov, J. A. Delettrez, A. V. Maximov, J. F. Myatt, W. Seka, A. Shvydky, S. Skupsky, and C. Stoeckl, *Phys. Plasmas* **17**, 122708 (2010).
 30. S. X. Hu, B. Militzer, V. N. Goncharov, and S. Skupsky, *Phys. Rev. Lett.* **104**, 235003 (2010); S. X. Hu, L. A. Collins, V. N. Goncharov, J. D. Kress, R. L. McCrory, and S. Skupsky, *Phys. Rev. E* **92**, 043104 (2015).
 31. V. N. Goncharov, in *Laser-Plasma Interactions and Applications*, edited by P. McKenna, D. Neely, R. Bingham, and D. A. Jaroszynski, Scottish Graduate Series (Springer, Switzerland, 2013), Chap. 7, pp. 135–183.
 32. V. N. Goncharov, O. V. Gotchev, E. Vianello, T. R. Boehly, J. P. Knauer, P. W. McKenty, P. B. Radha, S. P. Regan, T. C. Sangster, S. Skupsky, V. A. Smalyuk, R. Betti, R. L. McCrory, D. D. Meyerhofer, and C. Cherfils-Clérouin, *Phys. Plasmas* **13**, 012702 (2006).
 33. D. S. Clark *et al.*, *Phys. Plasmas* **21**, 112705 (2014).
 34. V. N. Goncharov, S. P. Regan, T. C. Sangster, R. Betti, T. R. Boehly, E. M. Campbell, J. A. Delettrez, D. H. Edgell, R. Epstein, C. J. Forrest, D. H. Froula, V. Yu. Glebov, D. R. Harding, S. X. Hu, I. V. Igumenshchev, F. J. Marshall, R. L. McCrory, D. T. Michel, J. F. Myatt, P. B. Radha, W. Seka, A. Shvydky, C. Stoeckl, W. Theobald, B. Yaakobi, and M. Gatu-Johnson, *J. Phys.: Conf. Ser.* **717**, 012008 (2016).
 35. A. Bose, K. M. Woo, R. Betti, E. M. Campbell, D. Mangino, A. R. Christopherson, R. L. McCrory, R. Nora, S. P. Regan, V. N. Goncharov, T. C. Sangster, C. J. Forrest, J. Frenje, M. Gatu Johnson, V. Yu. Glebov, J. P. Knauer, F. J. Marshall, C. Stoeckl, and W. Theobald, *Phys. Rev. E* **94**, 011201(R) (2016).
 36. I. V. Igumenshchev, V. N. Goncharov, F. J. Marshall, J. P. Knauer, E. M. Campbell, C. J. Forrest, D. H. Froula, V. Yu. Glebov, R. L. McCrory, S. P. Regan, T. C. Sangster, S. Skupsky, and C. Stoeckl, *Phys. Plasmas* **23**, 052702 (2016).
 37. R. C. Shah, B. M. Haines, F. J. Wysocki, J. F. Benage, J. Fooks, V. Glebov, P. Hakel, M. Hoppe, I. V. Igumenshchev, G. Kagan, R. C. Mancini, F. J. Marshall, D. T. Michel, T. J. Murphy, M. E. Schoff, C. Stoeckl, and B. Yaakobi, “Systematic Fuel Cavity Asymmetries in Directly Driven ICF Implosions,” submitted to *Physical Review Letters*.
 38. D. T. Michel, A. K. Davis, W. Armstrong, R. Bahr, R. Epstein, V. N. Goncharov, M. Hohenberger, I. V. Igumenshchev, R. Jungquist, D. D. Meyerhofer, P. B. Radha, T. C. Sangster, C. Sorce, and D. H. Froula, *High Power Laser Science and Engineering* **3**, e19 (2015).
 39. T. J. Murphy, *Phys. Plasmas* **21**, 072701 (2014).
 40. R. Betti and J. Sanz, *Phys. Rev. Lett.* **97**, 205002 (2006).
 41. I. V. Igumenshchev, V. N. Goncharov, W. T. Shmayda, D. R. Harding, T. C. Sangster, and D. D. Meyerhofer, *Phys. Plasmas* **20**, 082703 (2013).
 42. C. Stoeckl, M. Bedzyk, G. Brent, R. Epstein, G. Fiksel, D. Guy, V. N. Goncharov, S. X. Hu, S. Ingraham, D. W. Jacobs-Perkins, R. K. Jungquist, F. J. Marshall, C. Mileham, P. M. Nilson, T. C. Sangster, M. J. Shoup III, and W. Theobald, *Rev. Sci. Instrum.* **85**, 11E501 (2014).
 43. T. C. Sangster, V. N. Goncharov, R. Betti, P. B. Radha, T. R. Boehly, D. T. Casey, T. J. B. Collins, R. S. Craxton, J. A. Delettrez, D. H.

- Edgell, R. Epstein, C. J. Forrest, J. A. Frenje, D. H. Froula, M. Gatu-Johnson, V. Yu. Glebov, D. R. Harding, M. Hohenberger, S. X. Hu, I. V. Igumenshchev, R. Janezic, J. H. Kelly, T. J. Kessler, C. Kingsley, T. Z. Kosc, J. P. Knauer, S. J. Loucks, J. A. Marozas, F. J. Marshall, A. V. Maximov, R. L. McCrory, P. W. McKenty, D. D. Meyerhofer, D. T. Michel, J. F. Myatt, R. D. Petrasso, S. P. Regan, W. Seka, W. T. Shmayda, R. W. Short, A. Shvydky, S. Skupsky, J. M. Soures, C. Stoeckl, W. Theobald, V. Versteeg, B. Yaakobi, and J. D. Zuegel, *Phys. Plasmas* **20**, 056317 (2013).
44. I. V. Igumenshchev, D. H. Froula, D. H. Edgell, V. N. Goncharov, T. J. Kessler, F. J. Marshall, R. L. McCrory, P. W. McKenty, D. D. Meyerhofer, D. T. Michel, T. C. Sangster, W. Seka, and S. Skupsky, *Phys. Rev. Lett.* **110**, 145001 (2013).
45. D. H. Froula, T. J. Kessler, I. V. Igumenshchev, R. Betti, V. N. Goncharov, H. Huang, S. X. Hu, E. Hill, J. H. Kelly, D. D. Meyerhofer, A. Shvydky, and J. D. Zuegel, *Phys. Plasmas* **20**, 082704 (2013).
46. I. V. Igumenshchev, W. Seka, D. H. Edgell, D. T. Michel, D. H. Froula, V. N. Goncharov, R. S. Craxton, L. Divol, R. Epstein, R. Follett, J. H. Kelly, T. Z. Kosc, A. V. Maximov, R. L. McCrory, D. D. Meyerhofer, P. Michel, J. F. Myatt, T. C. Sangster, A. Shvydky, S. Skupsky, and C. Stoeckl, *Phys. Plasmas* **19**, 056314 (2012).